Electronic Supplementary Information to

Lattice dynamics in the conformational environment of multilayered hexagonal boron nitride (h-BN) results in peculiar infrared optical responses

Luigi Cigarini*, Michal Novotný, and František Karlický*

*Department of Physics, Faculty of Science, University of Ostrava, 30. dubna 22, 701 03 Ostrava, Czech Republic.**

(Dated: March 18, 2021)

List of provided supplemental data:

TS - Supplemental table.
S - Supplemental figure.

- TSI - Detailed parameters of all the calculations performed.
- TSII - Lattice parameters calculated with a selection of different methods.
- TSIII - Atomic coordinates of the symmetrical structures.
- S1 - PESs cuts for rigid sliding of h-BN planes from the AB' structure calculated with a selection of different methods.
- TSIV - Semi-empirical Born Q matrices and dielectric tensors calculated as explained in Sections III C and V E of the Main Text.
- TSV, TSVI - Phonon frequencies at the Γ point for the AB and AB' structures calculated with a selection of different methods.
- S2, S3, S4, S5 - Vibrational spectra for AB and AB' structures calculated with a selection of different methods.
- S6 - Sections of the valence charge density functions $\rho_{(PAW-PBE)}(\mathbf{r})$ of fictitious systems obtained as explained in Sections III C and V E of the Main Text, used to calculate the data reported in Table TSIV.
- S8 - Phonon energy dispersions calculated with the semi-empirical non-analytical corrections of Table TSIV.
- S9 - Ultrasoft PP, LDA energy dispersions of phonons (NA: numerical implementation US-LDA DFPT).

* luigi.cigarini@osu.cz, frantisek.karlicky@osu.cz

- S10 - NC PP, PBE, Tkatchenko-Scheffler corrected energy dispersions of phonons (NA: numerical implementation PAW-PBE [Set *a*] DFPT).

- S11 - NC PP, SCAN energy dispersions of phonons (NA: numerical implementation NC-SCAN DFPT).

- S14 - PAW PP, PBE, D2 vdW energy dispersions of phonons (NA: numerical implementation PAW-PBE [Set *b*] DFPT).

- S15, TSII, TSV, TSVI - Tests for the effects of the formal vdW corrections.

- S12, S13, S15 - Non-standard explorations of the potential energy hypersurfaces.

- S16, S17, S18 - Convergence studies.

I. CALCULATION PARAMETERS

TABLE TSI: Methods and calculation parameters used to obtain the results discussed in the text. Some of the employed settings, reported here, are motivated only by explorative purposes.

Code	General Calc. Setup					SCF Calc. of $\rho_x(r)$		FD IFC			
	PP	xc	Disp. Correction	$E_{cut.}$ (eV)	$E_{cut.\rho}$ (eV)	**k**-points grid	SCF Conv. (eV)	Supercell	**k**-points Grid	Displ. (Å)	SCF Conv. (eV)
QE	NC	PBE	TS	2041	8163	20×20×20	$1.36 \cdot 10^{-12}$	AA': 6×6×2 AB': 6×6×2 Others: 5×5×2	2×2×2	0.01	$1.36 \cdot 10^{-7}$
	NC	SCAN	-	2041	10885	20×20×20	$1.36 \cdot 10^{-12}$	6×6×2	2×2×2	0.01	$1.36 \cdot 10^{-7}$
	US	LDA	-	544	10885	20×20×20	$1.36 \cdot 10^{-12}$	AA': 6×6×2 A'B: 6×6×1 Others: 5×5×2	2×2×2	AB: 0.03 AB': 0.015 Others: 0.01	$1.36 \cdot 10^{-7}$
	PAW	PBE	D2 $^{Set\ a}$	544	10885	20×20×20	$1.36 \cdot 10^{-12}$	AB': 6×6×1 Others: 6×6×2	2×2×2	AB': 0.15 Others: 0.01 AB': No disp. correction	$1.36 \cdot 10^{-7}$
VASP	PAW	PBE	D2 $^{Set\ b}$ D3BJ TS	500	-	12×12×4	$1 \cdot 10^{-8}$	4×4×2	3×3×2	0.01	$1 \cdot 10^{-8}$
	PAW	SCAN	SCAN +rVV10	500	-	12×12×4	$1 \cdot 10^{-8}$	4×4×2	3×3×2	0.01	$1 \cdot 10^{-8}$

NC - Norm-conserving Troullier–Martins FHI PP [1–5], US - Vanderbilt Ultrasoft PP [6], TS - Tkatchenko-Scheffler dispersion correction [7], D2 - Grimme-D2 dispersion correction [8], PAW - Projector Augmented-Wave method [9, 10], SCAN - Strongly Constrained and Appropriately Normed semilocal density functional [11, 12], SCAN+rVV10 - SCAN + revised Vydrov–van Voorhis nonlocal correlation functional [13], D3BJ - Grimme-D3 dispersion correction with Becke-Johnson damping function [14], Set *a* and *b* - Internal references used in the text to indicate the specific settings reported in Rows 4 and 5 of this table.

II. DESCRIPTION OF THE POTENTIAL ENERGY SURFACES

The potential energy surfaces (PESs) cuts reported in this work (Figure 3 in the Main Text and Figure S1 in the Electronic Supplementary Information [E.S.I.]) are calculated employing a selection of different methods and generated by parallel sliding of the contiguous h-BN planes with respect to each other, keeping the optimized lattice parameters and displacing only the atomic positions. The reported results span intervals from -0.5 Å to 0.5 Å in the x and y directions with respect to the symmetrical structures. Note that we used optimized structural parameters for each different plot (see E.S.I. [Table TSII]) and the absolute energies of the symmetrical points are, therefore, inconsistent among the plots themselves (the reason being that, e.g., the AA' structure obtained shifting from the fully optimized AB' comes in a different periodicity with respect to a fully relaxed AA').

The shape of the PES confirms the stability of the AA' and AB symmetrical structures by being true minima, which is backed up by the comparison of the total energies. The AB configuration appears to be the most stable one with an energy difference to the next most stable stacking between 0.22 meV/atom (NC-PBE-TS) to 2.04 meV/atom (PAW-PBE-TS). The PAW-PBE-TS predicted the AB' structure to be the most stable one while AB being second with an energy difference in the minimum of 0.76 meV/atom. The total energy of the AB' configuration ranges from 1.81 meV/atom (NC-PBE-TS) to 5.37 meV/atom (QE-PAW-PBE-D2) above the AB minimum. The values calculated with QE-PAW-PBE-D2, and to a lesser extent NC-SCAN, significantly exceed the energy differences obtained from other methods. The local minimum of AB' is located in a prominently flat valley (or a soft groove in NC-SCAN and US-LDA). Although the AA' configuration is located at (-0.33,0.33) Å from the AB' local minima and is easily reachable upon simple sliding, the AB' stacking configuration seems to be metastable, leading to possible dynamical stability related interpretations of the experimental data [15, 16]. This is also supported by the cozy shape of the PES in the vicinity of the AB' minimum particularly prominent in the NC-SCAN data and reported in more detail in the E.S.I. (Figure S1, uppermost panel). It is not possible to get to the AB ($P3m1$) stacking by linearly sliding the planes from the AA' or AB' ($P6_3/mmc$) local minima. A 60° rotational movement is instead necessary, due to the different symmetry of the lattice space group. The AA and A'B configurations are located on local max-

ima stationary points (Fig. 3 of the Maint Text), implying instability of these stacking variants. The energy drop is strongly dependent on the theoretical methodology: the NC-PBE-TS method calculates significantly lower total energies for these unstable configurations, while the higher energy results are obtained with QE-PAW-PBE-D2.

III. DESCRIPTION OF THE PHONONIC MODES

We calculated energy dispersion functions of the phononic modes for all the examined stacking variants with an extremely wide selection of methods. The results are shown in Fig. 4 of the Main Text and in the E.S.I.

Besides the three acoustic modes, the two plane sliding modes are easily recognizable below 100 cm^{-1} (E_{2g}) at the Γ point in all the dispersion diagrams, becoming imaginary in the unstable ones as indicated by the potential energy surfaces. A symmetrical "plane bumping" mode along the z direction (B_{1g}) is distinguishable from 150 cm^{-1} to 200 cm^{-1}. At about 800 cm^{-1} at the Γ point, two "umbrella movement" modes (symmetrical and asymmetrical) can be observed. The asymmetrical one (A_{2u}) is IR active and we denote it here as Peak 1. In Figure 5 of the Main Text we report a graphical representation of the resulting displacements for the IR active modes at the Γ point in the AA' system. The A_{2u} mode is showed in Panel c. It consists by out-of-plane displacements of boron and nitrogen atoms in opposite directions (asymmetric bouncings) and interplanar van der Waals interactions are highly involved here. Finally, the higher energetic group of phonons is composed by four modes (higher than 1300 cm^{-1} at the Γ point) and arises from B-N stretching modes. The high energy results primarily from the deformation of in-plane covalent interactions. The E_{2g} mode is symmetrical and Raman active while the E_{1u} mode, composed by in-plane asymmetric stretching movements, is IR active and LO-TO split by the macroscopic electric field in two perpendicular branches. These two signals generally overlap each other in experimental spectra and we denote them, here, as a singular Peak 2. The displacement vectors relevant to it are represented in Panels a and b of Figure 5 in the Main Text.

The stable and unstable structures can also be distinguished by the behaviour of the B_{1g} and A_{2u} modes (at $\sim$ 800cm^{-1} at the Γ point) in the $A-\Gamma$ direction where the unstable structures exhibit a full degeneracy of the two modes, in contrast to the split seen in the stable stackings. The five stackings have otherwise an almost identical phonon structure. Concerning the IR and Raman active modes, the two most stable stackings (AA'

and AB) exhibit identical phonon frequencies whereas the AB' presents slightly higher vibrational energies leading to different optical activity. We have calculated the phonon dispersion spectra with various dispersion correction methods (see Fig. 4 and Table 2 in the Main Text and data reported in the E.S.I. [Tables TSV, TSVI, Figures S10, S14, S16, S17, S18]). One would assume that due to the nature of the system in study different approaches to weak binding would have a significant impact on the phononic structure but this is not the case. The effect of the van der Walls correction can be seen only for the B_{1g} mode arising from the planar shifts along the vertical axis $\sim$ 120-200 cm^{-1} as well as the E_{2g} sliding of the planes along each other $\sim$ 40-60 cm^{-1}. Both of these modes do not induce a change in the dipole moment and therefore will not be visible in the IR spectrum. When compared with experimental results, as shown in Tab. 2 Main Text for the AA' variant and in the E.S.I. (Tables TSV, TSVI) for the AB and AB', all the methods agree well on a qualitative level.

Lattice constants

TABLE TSII: Lattice constants (in Å) for the five analyzed conformations of h-BN, resulting from geometrical optimization with different theoretical approaches. Details about theoretical and computational methods are specified in the relevant sections: Methods Section of the Main Text and Table TSI of the Electronic Supplementary Information (E.S.I.).

			AA'	AB	AB'	A'B	AA
		Method	$P6_3/mmc$	$P3m1$	$P6_3/mmc$	$P6_3/mmc$	$P\bar{6}m2$
a	VASP	PBE-D2 [1] (b)	2.509	2.508	2.508	2.508	2.508
		PBE-D3BJ [1]	2.507	2.507	2.506	2.506	2.506
		PBE-TS [1]	2.505	2.505	2.504	2.504	2.503
		SCAN+rVV10 [1]	2.497	2.497	2.496	2.495	2.495
	QE	PBE-D2 [1] (a)	2.513	2.513	2.510	2.510	2.510
		LDA [2]	2.490	2.490	2.490	2.490	2.490
		PBE-TS [3]	2.504	2.501	2.501	2.501	2.501
		SCAN [3]	2.506	2.506	2.504	2.504	2.504
c	VASP	PBE-D2 [1] (b)	6.159	6.096	6.214	6.608	6.699
		PBE-D3BJ [1]	6.567	6.547	6.606	6.927	6.968
		PBE-TS [1]	6.642	6.625	6.533	6.864	6.843
		SCAN+rVV10 [1]	6.379	6.364	6.43	6.747	6.796
	QE	PBE-D2 [1] (a)	6.178	6.124	6.233	6.667	6.762
		LDA [2]	6.490	6.450	6.531	7.074	7.155
		PBE-TS [3]	6.653	6.613	6.708	7.277	7.386
		SCAN [3]	6.504	6.463	6.558	7.101	7.182

[1] - Projector Augmented Wave PP

[2] - Ultrasoft PP

[3] - Norm-conserving PP

Atomic coordinates of the symmetrical structures

TABLE TSIII: Coordinates of the atomic centres in the five studied geometries. The coordinates are expressed in units of the hexagonal crystal lattice (reported in Tab. TSII).

		x	y	z
AA'	**B**	0.000000000	0.000000000	0.000000000
	B	0.333333333	0.666666667	0.500000000
	N	0.333333333	-0.333333333	0.000000000
	N	0.000000000	0.000000000	0.500000000
AB	**B**	0.000000000	0.000000000	0.000000000
	B	0.666666667	-0.666666667	0.500000000
	N	0.333333333	-0.333333333	0.000000000
	N	0.000000000	0.000000000	0.500000000
AB'	**B**	0.000000000	0.000000000	0.000000000
	B	0.000000000	0.000000000	0.500000000
	N	0.333333333	-0.333333333	0.000000000
	N	0.666666667	-0.666666667	0.500000000
A'B	**B**	0.666666667	-0.666666667	0.500000000
	B	0.333333333	-0.333333333	0.000000000
	N	0.000000000	0.000000000	0.000000000
	N	0.000000000	0.000000000	0.500000000
AA	**B**	0.000000000	0.000000000	0.000000000
	B	0.000000000	0.000000000	0.500000000
	N	0.333333333	-0.333333333	0.000000000
	N	0.333333333	0.666666667	0.500000000

AB' structure

Potential energy surfaces

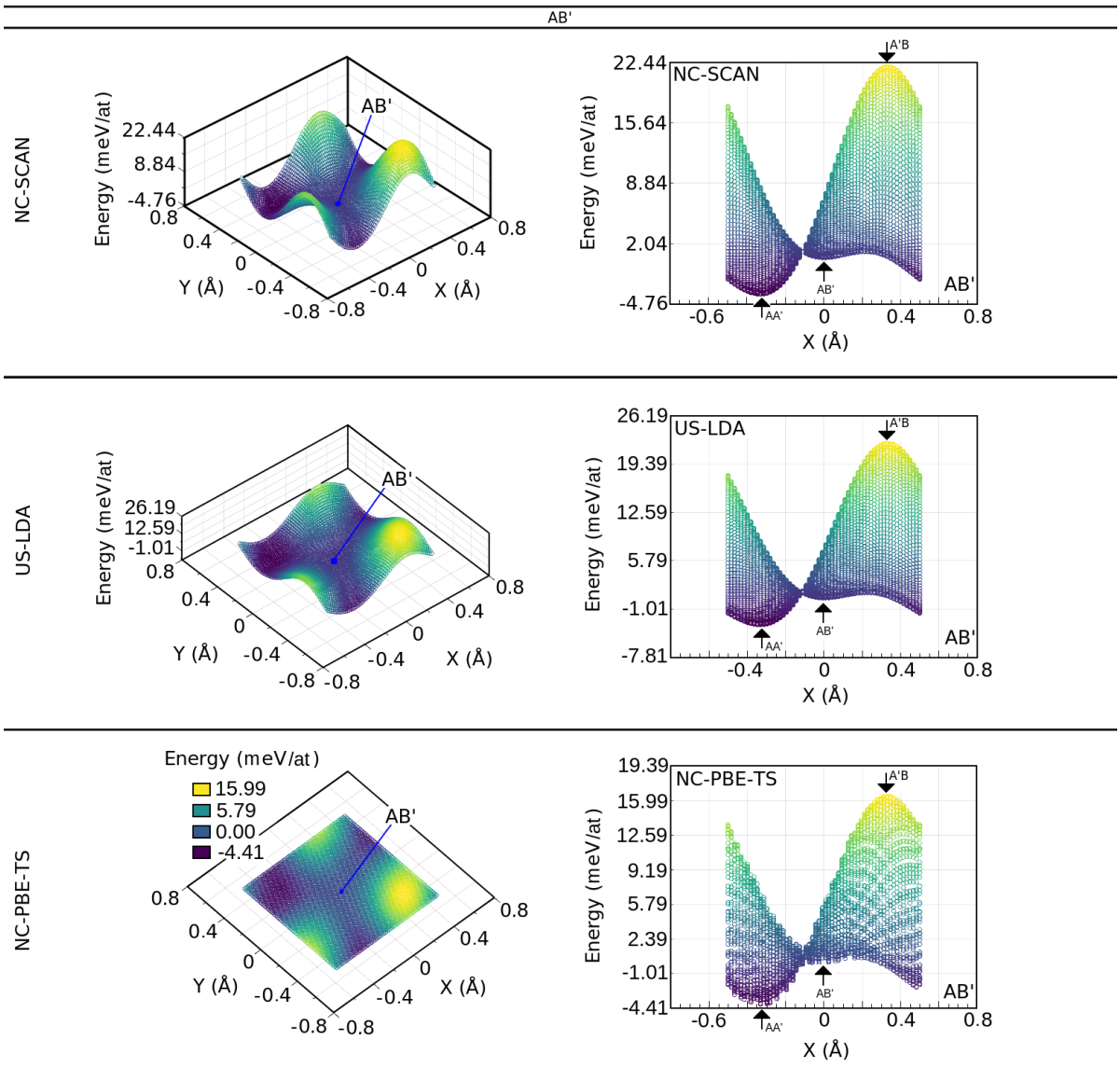

FIG. S1: Potential energy surfaces (PESs) cuts calculated, with different theoretical implementations, upon rigid sliding movements of contiguous h-BN planes, keeping fixed the optimized cell structural parameters obtained for the **AB' symmetrical settlement** with each different method (reported in Table TSII). For Computational details see the relevant Methods Section of the Main Text and Table TSI of the Electronic Supplementary Information (E.S.I.).

Semi-empirical Born Q matrices and dielectric tensors

TABLE TSIV: Semi-empirically obtained non-analytical parts of the dynamical matrices for the three h-BN stable systems, calculated numerically with DFPT and PAW-PBE (Set a) on fictitious 32.94% c shortened systems. The shortening operation has been performed with respect to optimized geometry obtained with PAW-PBE-D2 (Set a, reported in Table TSII) and no further geometrical optimization (atomic centers in relative positions with respect to the cell parameters). See Sections 3.4 and 2.3 of the Main Text of this work.

AA'				**AB**				**AB'**			
Dielectric tensor $\epsilon^{(\infty)}$				Dielectric tensor $\epsilon^{(\infty)}$				Dielectric tensor $\epsilon^{(\infty)}$			
	x	y	z		x	y	z		x	y	z
x	5.410	0.000	0.000	x	7.010	0.000	0.000	x	67.994	-26.684	0.000
y	0.000	5.410	0.000	y	0.000	7.011	0.000	y	-26.684	37.182	0.000
z	0.000	0.000	9.578	z	0.000	0.000	7.615	z	0.000	0.000	9.046
Born Q matrix elements $Q_s^{\alpha\beta}$ (e)				Born Q matrix elements $Q_s^{\alpha\beta}$ (e)				Born Q matrix elements $Q_s^{\alpha\beta}$ (e)			
	x	y	z		x	y	z		x	y	z
B (0,0,0)				B (0,0,0)				B (0,0,0)			
x	2.414	0.000	0.000	x	2.351	0.000	0.000	x	4.525	-0.402	0.000
y	-0.022	2.426	0.000	y	-0.023	2.364	0.000	y	-0.444	4.086	0.000
z	-0.008	0.000	4.284	z	-0.008	0.000	3.552	z	-0.014	0.002	1.958
B (1/3,2/3,1/2)				B (2/3,-2/3,1/2)				B (0,0,1/2)			
x	2.414	0.000	0.000	x	2.992	0.000	0.000	x	4.525	-0.402	0.000
y	-0.022	2.426	0.000	y	-0.025	3.007	0.000	y	-0.444	4.086	0.000
z	-0.008	0.000	4.284	z	-0.009	0.000	2.086	z	-0.014	0.002	1.958
N (1/3,-1/3,0)				N (1/3,-1/3,0)				N (1/3,-1/3,0)			
x	-2.412	0.000	0.000	x	-2.699	0.000	0.000	x	-4.546	0.424	0.000
y	-0.007	-2.409	0.000	y	-0.008	-2.695	0.000	y	0.420	-4.055	0.000
z	-0.002	0.000	-4.270	z	-0.003	0.000	-2.656	z	-0.001	0.000	-1.994
N (0,0,1/2)				N (0,0,1/2)				N (2/3,-2/3,1/2)			
x	-2.412	0.000	0.000	x	-2.642	0.000	0.000	x	-4.546	0.424	0.000
y	-0.007	-2.409	0.000	y	-0.004	-2.640	0.000	y	0.420	-4.055	0.000
z	-0.002	0.000	-4.270	z	-0.002	0.000	-3.023	z	-0.001	0.000	-1.994

AB structure

Phonon frequencies at the Γ point

TABLE TSV: Phonon frequencies at the Γ point (in cm^{-1}) for the h-BN **AB stacking** as calculated by different theoretical approaches and software implementations and compared with experimental values taken from literature. The NA part of the dynamical matrix is calculated adopting numerically DFPT effective charges and dielectric tensors, where not differently specified, with the same method of the IFC. For Computational details see the relevant Methods Section of the Main Text and Table TSI of the Electronic Supplementary Information.

	VASP					QE				
Mode	PBE[1]	PBE-D2[1] (*b*)	PBE-D3BJ[1]	PBE-TS[1]	SCAN +rVV10 [1]	LDA[2]	PBE-D2[1] (*a*)	PBE-TS[3]	PBE-TS[3] NA: PAW-PBE[1]	Experiment
E_{2g}**	45	45	45	43	103	53	71	53	53	51 [23]
	45	45	45	43	107	53	71	57	57	
B_{1g}	125	81	118	150	107	113	177	149	149	-
A_{2u}*	751	748	750	755	766	758	731	763	763	767-810 [17–22, 24]
B_{1g}	798	794	798	802	821	812	793	810	810	-
E_{2g}**	1357	1359	1356	1343	1378	1386	1350	1350	1350	1369-1376 [23–25]
	1359	1362	1359	1346	1383	1390	1357	1354	1354	
E_{1u}*	1360	1362	1360	1346	1385	1389	1356	1353	1353	1338-1404 [17–22, 24]
E_{1u}*	1589	1591	1589	1576	1622	1613	1588	1576	1573	1616 [24]

[1] - Projector Augmented-Wave PP, [2] - Ultrasoft PP, [3] - Norm-conserving PP

* - IR active modes

** - Raman active modes

AB' structure

Phonon frequencies at the Γ point

TABLE TSVI: Phonon frequencies at the Γ point (in cm^{-1}) for the h-BN **AB' stacking** as calculated by different theoretical approaches and software implementations and compared with experimental values taken from literature. The NA part of the dynamical matrix is calculated adopting numerically DFPT effective charges and dielectric tensors, where not differently specified, with the same method of the IFC. See Computational details and Methods Sections in the Main Text of this work and Table TSI of the Electronic Supplementary Information.

	VASP					QE					
Mode	PBE[1]	PBE-D2[1] (*b*)	PBE-D3BJ[1]	PBE-TS[1]	SCAN +rVV10 [1]	LDA[2]	PBE-D2[1] (*a*)	PBE-TS[3]	PBE-TS[3] NA: PAW-PBE[1]	SCAN[3]	Experiment
E_{2g}**	36	35	36	45	121	40	51	60	60	40	51 [23]
	36	35	36	45	121	41	52	62	62	41	
B_{1g}	128	95	121	154	153	110	174	138	138	109	-
A_{2u}*	756	752	756	761	774	767	750	771	771	752	767-810 [17–22, 24]
B_{1g}	796	794	795	795	824	810	794	804	804	795	-
E_{2g}**	1357	1360	1357	1359	1379	1386	1390	1352	1352	1373	1369-1376 [23–25]
	1360	1362	1360	1362	1379	1389	1396	1354	1354	1376	
E_{1u}*	1360	1362	1360	1362	1380	1389	1394	1354	1354	1376	1338-1404 [17–22, 24]
E_{1u}*	1586	1588	1586	1588	1620	1608	1616	1575	1569	1594	1616 [24]

[1] - Projector Augmented-Wave PP, [2] - Ultrasoft PP, [3] - Norm-conserving PP

* - IR active modes

** - Raman active modes

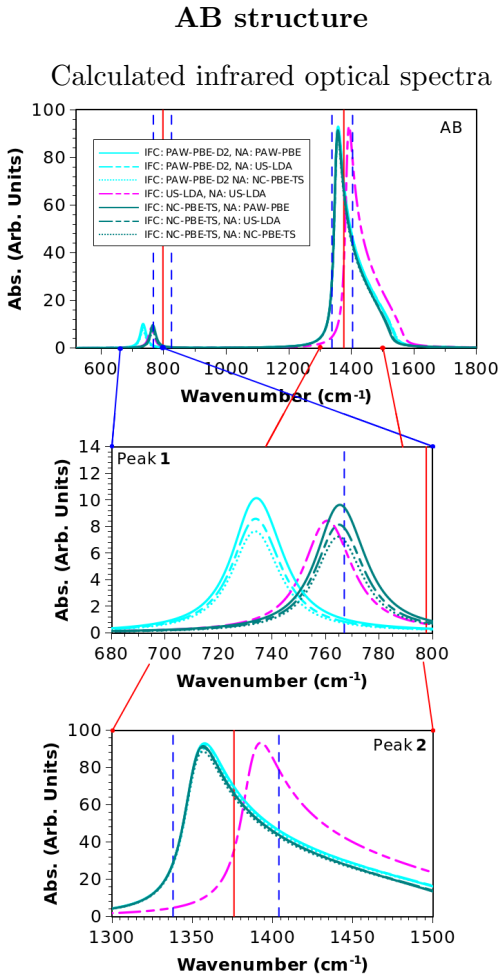

FIG. S2: Vibrational spectra calculated for the h-BN **AB stacking configuration** with different theoretical approaches, as described in legend (for PAW-PBE we use Set *a*). In insets, details of Peak 1 and Peak 2 regions are showed. Red solid vertical lines indicate the average experimental peak values and blue vertical dotted lines indicate the range limits of measured high absorptions in the six experimental references [17–22]. Computational details and methods are thoroughly examined in the relevant section in the Main Text of this work and Table TSI of the E.S.I.

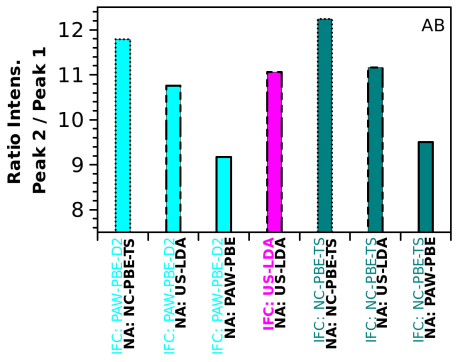

FIG. S3: Ratios between the intensities of absorption of the two IR active peaks of vibrational spectra calculated for the simulated h-BN **AB stacking structure** with different theoretical implementations (for PAW-PBE we use Set *a*). Computational details and theoretical information on Methods are provided in the relevant Section in the Main Text of this work and Table TSI of the E.S.I.

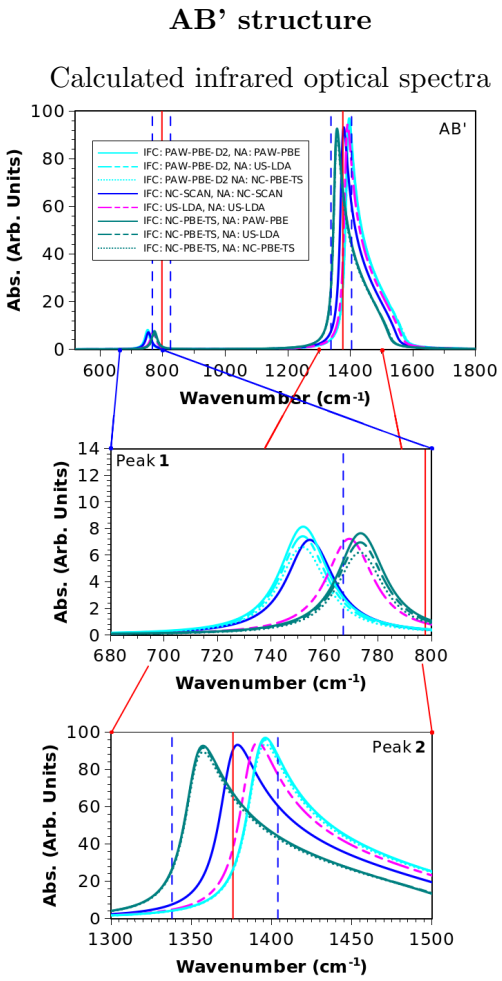

FIG. S4: Vibrational spectra calculated for the h-BN **AB' stacking configuration** with different theoretical approaches, as described in legend (for PAW-PBE we use Set *a*). In insets, details of Peak 1 and Peak 2 regions are showed. Red solid vertical lines indicate the average experimental peak values and blue vertical dotted lines indicate the range of the experimental data for the two peak frequencies, as gathered from the six experimental references [17–22]. Computational details and theoretical information are provided in the Methods Section of the Main Text and Table TSI of the E.S.I.

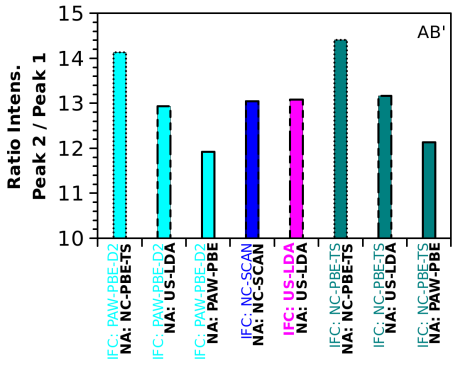

FIG. S5: Ratios between the intensities of absorption of the two IR active peaks of vibrational spectra calculated for the simulated h-BN **AB' stacking structure** with different theoretical implementations (for PAW-PBE we use Set *a*). See the computational details in the Methods Section of the Main Text and Table TSI of the E.S.I.

Charge density functions $\rho^{fict.}_{(PAW-PBE)}(\mathbf{r})$ of the h-BN fictitious systems, $\mathbf{r} \equiv (R, \theta, \phi)$.

Used to obtain the semi-empirical Born Q matrices and dielectric tensors reported in Table TSIV.

$$\left[R < R_{HP}\right] \wedge \left[\theta \leq \theta_{HP}\right] \implies \rho^{fict.}_{(PAW-PBE)}(\mathbf{r}) \approx \rho_{(Q)}(\mathbf{r}),$$

see Sections 2.3, 3.4 and Appendix of the Main Text.

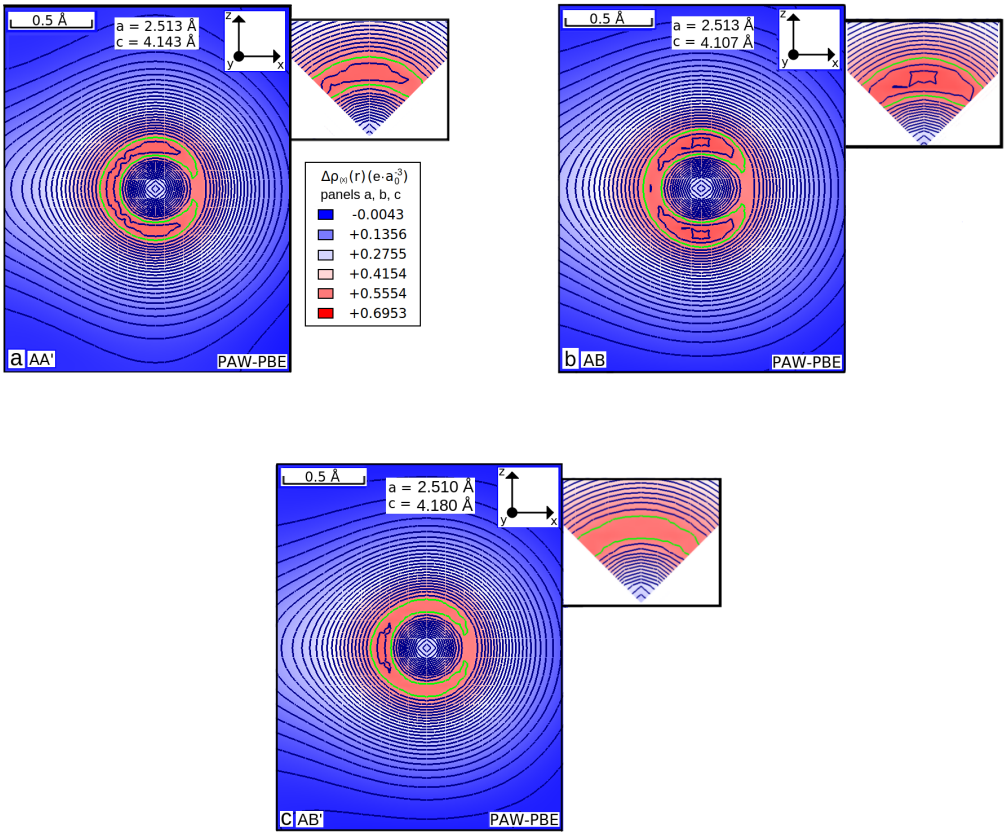

FIG. S6: Nitrogen xz sections of the valence charge density functions $\rho^{fict.}_{(PAW-PBE)}(\mathbf{r})$ (Set a, recalculated with a $40 \times 30 \times 20$ Monkhorst-Pack $\mathbf{k}$-points grid in the first Brillouin zone of an equivalent orthorhombic unit cell, see Methods section in the Main Text and Table TSI of the E.S.I.) calculated in h-BN fictitious systems obtained as explained in Sections 2.3 and 3.4 of the Main Text, by applying the 32.94% shortening percentage to the c parameter in the z direction from fully optimized (PAW-PBE-D2 [Set a]) h-BN structures (AA', AB and AB') and no further geometrical optimization (nuclei in relative positions). Nitrogen nuclei in the centres of the panels. The 0.5718 $e \cdot a_0^{-3}$ isolines of charge density are highlighted in green. In insets, details of polar cones sections. Close-up details are reported in Figure S7.

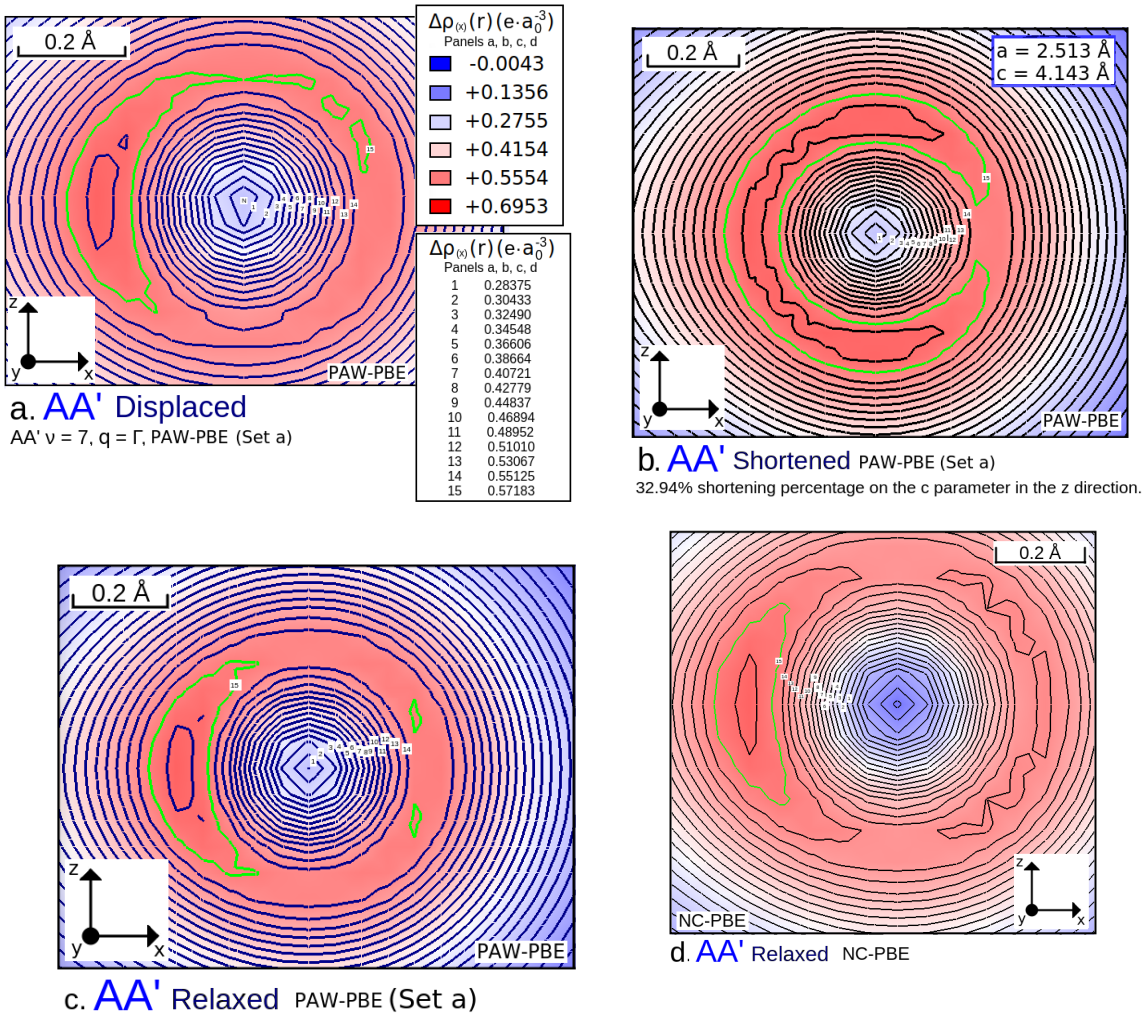

FIG. S7: Nitrogen xz sections, detailed maps for a set of real space valence charge density functions in selected h-BN AA' structures. Nitrogen nuclei are in the centres of the contour lines zones, approximately in the middle of the panels. The 0.5718 $e \cdot a_0^{-3}$ isolines of charge density are highlighted in green. The legends attached to Panel a inform about the four panels.

Phonon energy dispersions with semi-empirical non-analytical corrections

Semi-empirical NA parameters reported in Table TSIV

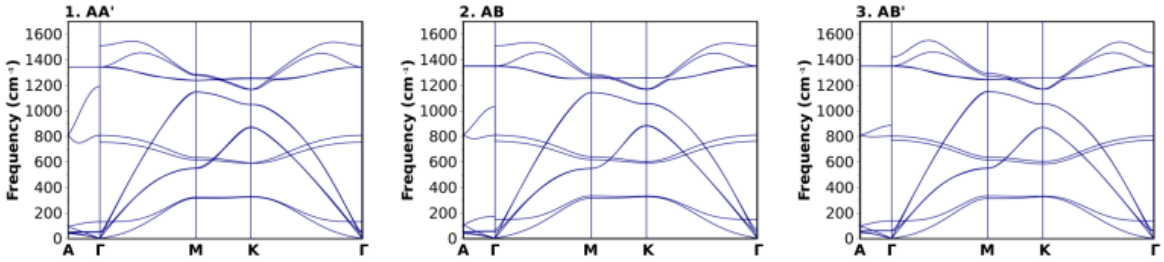

FIG. S8: Comparison of the phonon energy dispersions along high symmetry directions in the first Brillouin zone for the three stable h-BN systems. The IFC matrices are calculated by Finite Displacements method with DFT PBE functional, NC pseudopotential approximations and TS dispersion corrections (see Methods section of the Main Text and Table TSI of the E.S.I.). **The NA parts (reported in Table TSIV) are semi-empirically obtained by DFPT PAW-PBE (Set a, see Methods section of the Main Text and Table TSI of the E.S.I.) on fictitious systems shortened on the c parameter of 32.94% with respect to the optimized PAW-PBE-D2 (Set a) geometry and no further geometrical optimization from PAW-PBE-D2 (Set a) optimal** (atomic centers in relative positions with respect to the cell parameters). See Sections 2.3 and 3.4 of the Main Text of this work.

Ultrasoft PP, LDA energy dispersions of phonons

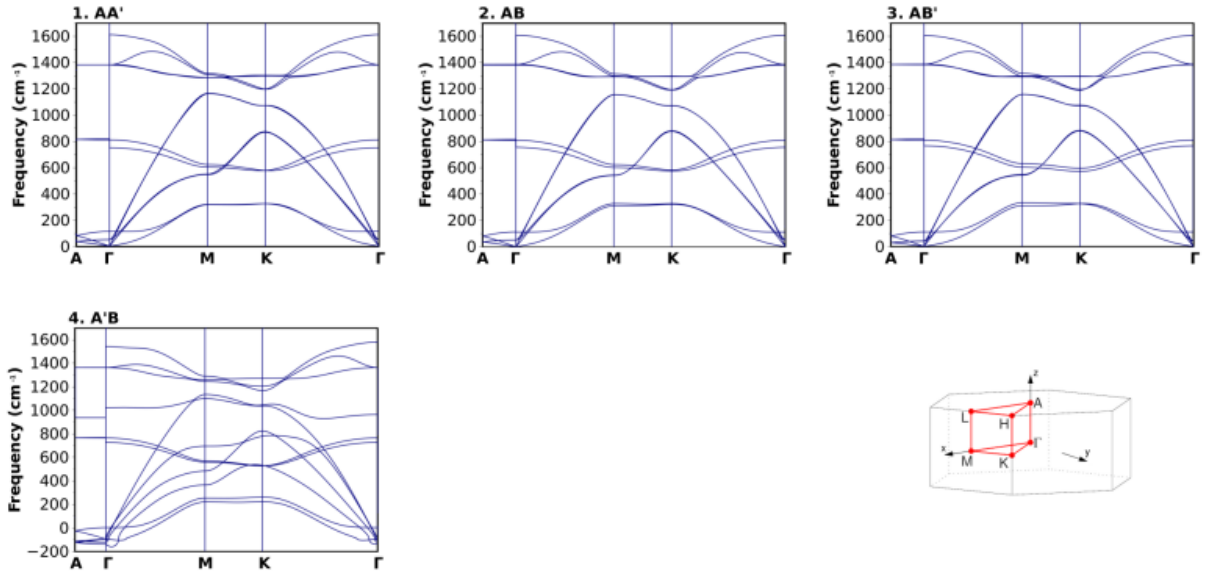

FIG. S9: Comparison of the phonon energy dispersions along high symmetry directions in the first Brillouin zone for four differently stacked h-BN systems. The IFC matrices are calculated by Finite Displacements method with **DFT LDA functional, US pseudopotential approximations**. The NA parts of the dynamical matrices are calculated adopting numerically US-LDA DFPT effective charges and dielectric tensors. Computational details and theoretical information are provided in the Methods Section of the Main Text and Table TSI of the E.S.I.

Norm-conserving PP, PBE, Tkatchenko-Scheffler vdW energy dispersions of phonons

NA: PAW-PBE (Set *a*) DFPT

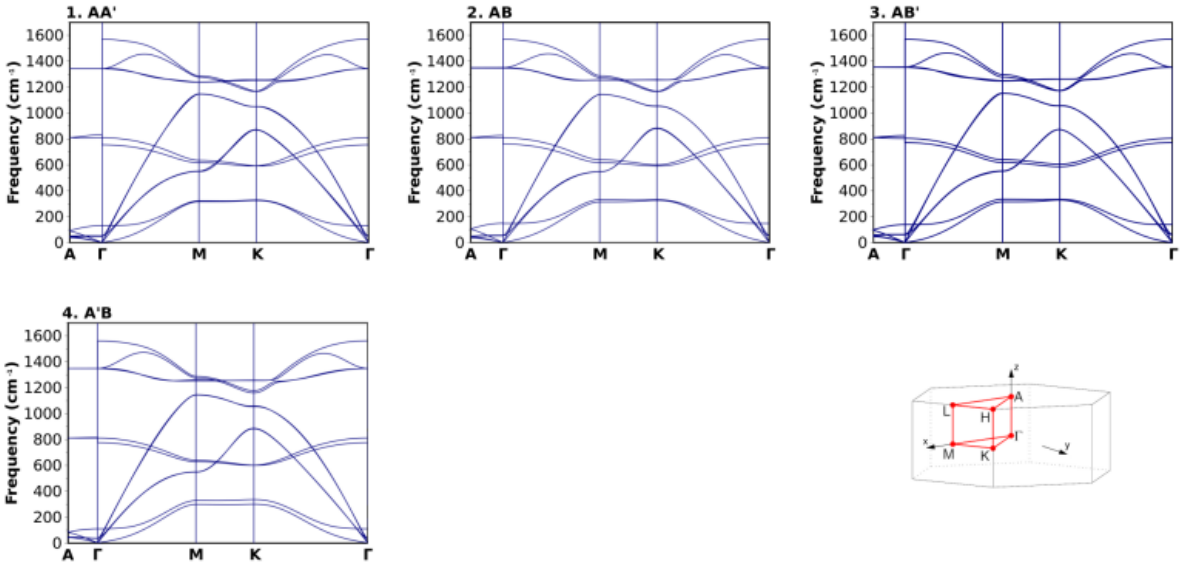

FIG. S10: Comparison of the phonon energy dispersions along high symmetry directions in the first Brillouin zone of four differently stacked h-BN systems. The IFC matrices are calculated by Finite Displacements method with **DFT PBE functional, NC pseudopotential approximations and TS dispersion corrections**. The NA parts of the dynamical matrices are calculated adopting numerically the resulting PAW-PBE (Set *a*) DFPT effective charges and dielectric tensors. See further computational details and theoretical information in the Methods Section of the Main Text and Table TSI of the E.S.I.

Norm-conserving PP, SCAN energy dispersions of phonons

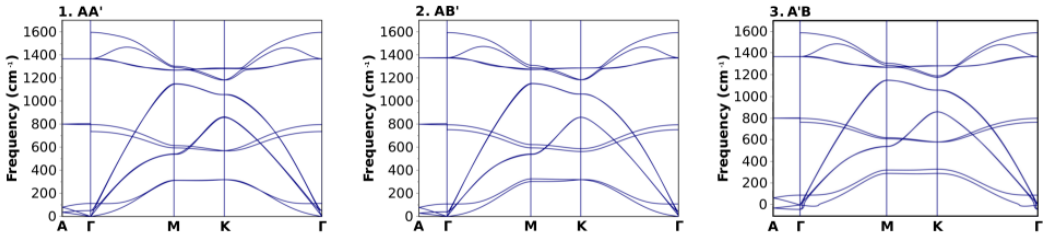

FIG. S11: Comparison of the phonon energy dispersions along high symmetry directions in the first Brillouin zone of three differently stacked h-BN systems. The IFC matrices are calculated by Finite Displacements method with **DFT SCAN functional and NC pseudopotential approximations**. The NA parts of the dynamical matrices are calculated adopting numerically the results of NC-SCAN DFPT effective charges and dielectric tensors. See further Computational details and theoretical information in the Methods Section of the Main Text and Table TSI of the E.S.I.

AA structure

Non-standard explorations of the potential energy hypersurface

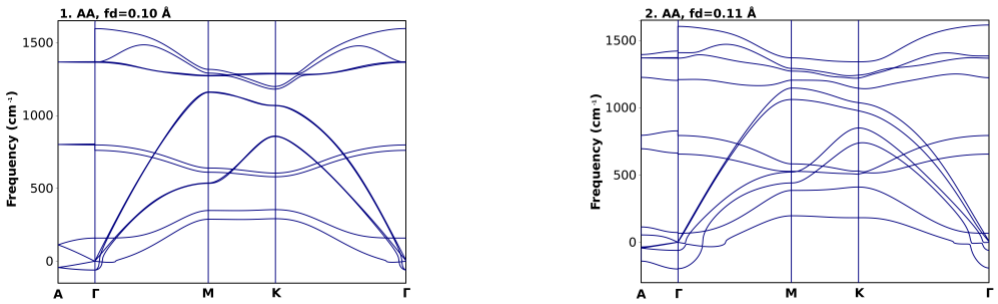

FIG. S12: Non-standard explorations of the potential energy hypersurface of the h-BN **AA structure**. Phonon eigenvalues obtained from the diagonalization of a dynamical matrix in which the IFC results from long-range finite displacements. Supercell 6×6×1. **Finite displacements (1) 0.10 Å, (2) 0.11 Å**. Cell parameters obtained from PAW-PBE-D2 (Set *a*, Table TSII). **No van der Waals dispersion correction in the FD SCF calculations**. The NA part of the dynamical matrix is calculated adopting numerically PAW-PBE (Set *a*) DFPT effective charges and dielectric tensors. All the other parameters as reported in E.S.I., Table TSI, Set *a*. Interesting hints come from the comparison of these unstable structures with the AB' scheme reported in Fig. 4 of the Main Text, which is obtained with the same theoretical implementation (Set *a*, Table TSI of the E.S.I.), but longer-range displacements of 0.15 Å.

A'B structure

Non-standard explorations of the potential energy hypersurface

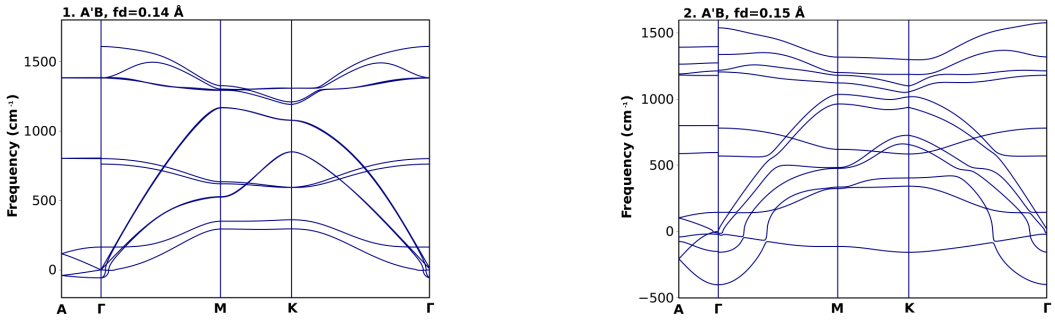

FIG. S13: Non-standard explorations of the potential energy hypersurface of the h-BN **A'B structure**. Phonon eigenvalues obtained from the diagonalization of a dynamical matrix in which the IFC results from long-range finite displacements. Supercell 6×6×1. **Finite displacements (1) 0.14 Å, (2) 0.15 Å**. Cell parameters obtained from PAW-PBE-D2 (Set *a*, Table TSII). **No van der Waals dispersion correction in the FD SCF calculations**. The NA part of the dynamical matrix is calculated adopting numerically PAW-PBE (Set *a*) DFPT effective charges and dielectric tensors. All the other parameters as reported in E.S.I., Table TSI, Set *a*. Interesting hints come from the comparison of these unstable structures with the AB' scheme reported in Fig. 4 of the Main Text, which is obtained with the same theoretical implementation (Set *a*, Table TSI of the E.S.I.), but longer-range displacements of 0.15 Å.

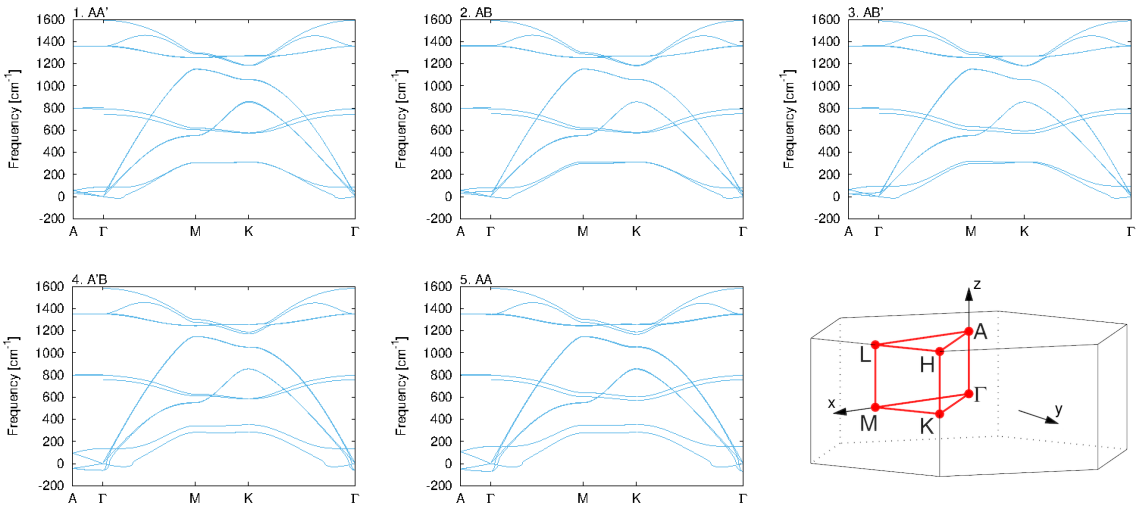

FIG. S14: Comparison of the phonon energy dispersions along high symmetry directions in the first Brillouin zone for the five considered differently stacked h-BN systems. The IFC matrices are calculated by Finite Displacements method with **FD of 0.01 Å, DFT PBE functionals, PAW pseudopotential approximations, Grimme-D2 dispersion corrections (VASP code. Set *b*, E.S.I. Table TSI)**. Cell parameters obtained with the same implementation PAW-PBE-D2 (Set *b*, E.S.I. Table TSII). The NA parts of the dynamical matrices are calculated adopting numerically the resulting PAW-PBE (Set *b*) DFPT effective charges and dielectric tensors. See further Computational details and theoretical information in the Methods Section of the Main Text and Table TSI of the E.S.I. Interesting hints come from the comparison, in view of the different computational implementations, of these schemes with the ones reported in Fig. 4 of the Main Text. Consider the different FD lengths used for the AB' structure (and compare also the AA and A'B non-standard explorations reported in the present E.S.I.).

A'B structure optimized without vdW corrections

Phonon energy dispersions

with a non-standard exploration of the potential energy hypersurface

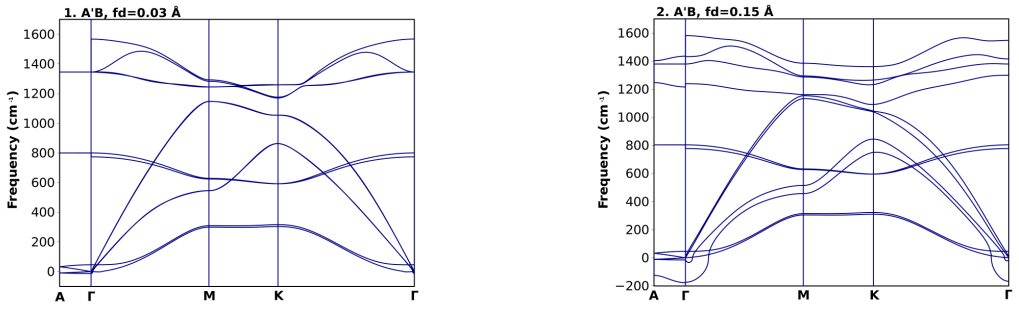

FIG. S15: Phonon energy dispersions along high symmetry directions in the first Brillouin zone for the h-BN **A'B structure**. **Cell parameters obtained from PAW-PBE (Set *a*) calculations (without vdW dispersion corrections): a=2.51 Å, c=8.20 Å**. **No van der Waals dispersion correction in the FD SCF calculations**. Supercell 6×6×1. **Finite displacements: (1) 0.03 Å, (2) 0.15 Å**. The results reported in panel 2 represent a non-standard way to explore the potential energy hypersurface of the structure. In fact, the eigenvalues are obtained from the diagonalization of a dynamical matrix resulting from untypical long-range finite displacements (0.15 Å). The NA part of the dynamical matrix is calculated adopting numerically PAW-PBE (Set *a*) DFPT effective charges and dielectric tensors. All the other parameters as reported in E.S.I. Table TSI, Set *a*.

Convergence study for the finite displacement value in FD SCF calculations

AA' structure

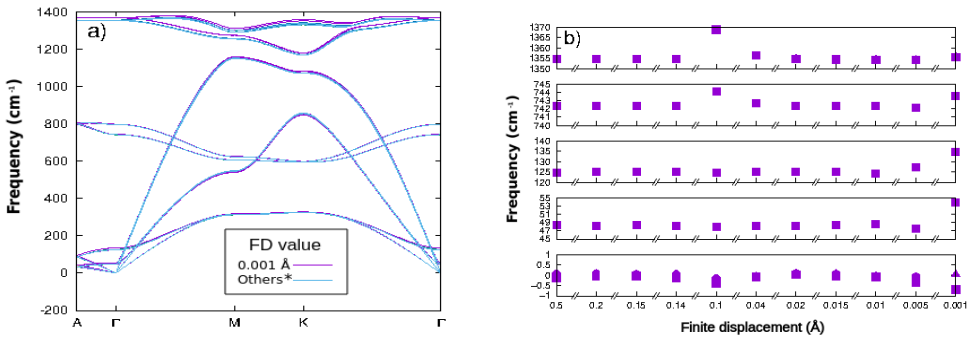

FIG. S16: Evolution of the phonon frequencies (a) along high symmetry directions in the first Brillouin zone and (b) in the Γ point, for the h-BN AA' structure (cell parameters obtained with PAW-PBE-D3BJ, reported in Table TSII, supercell size of $2 \times 2 \times 1$ unit cells), obtained with a set of different finite displacement values. Calculations performed with PAW-PBE and D3BJ van der Waals dispersion correction, see computational details in E.S.I. Table TSI.

*Other tested values: 0.005 Å, 0.01 Å, 0.015 Å, 0.02 Å, 0.04 Å, 0.1 Å, 0.14 Å, 0.15 Å, 0.2 Å, 0.5 Å (the results are superimposable in Panel *a*, showed as light blue lines).

Convergence study for the xy planar supercell size in FD SCF calculations

AA' Structure

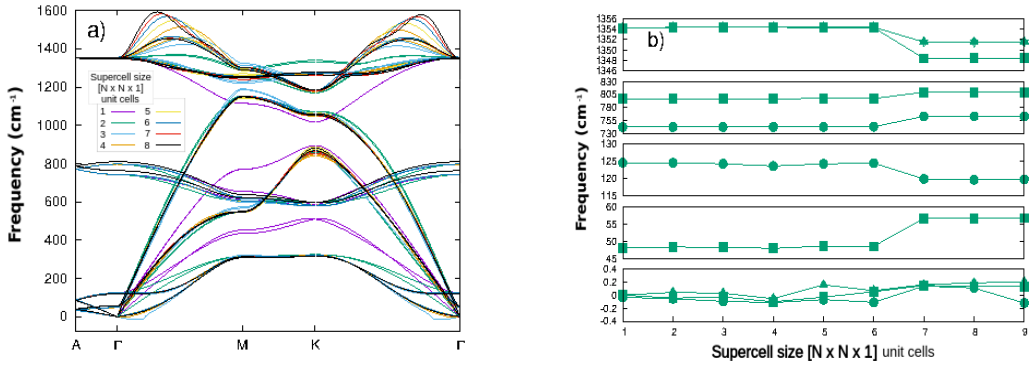

FIG. S17: Phonon energy dispersions for the h-BN AA' structure with varying supercell size in the in-plane xy directions (a) along high symmetry directions in the first Brillouin zone and (b) in the Γ point. Calculations performed with PAW-PBE and D3BJ van der Waals dispersion correction, FD value of 0.015 Å, see further information and computational details in E.S.I. Table TSI (cell parameters obtained with PAW-PBE-D3BJ, reported in Table TSII).

Convergence study for the z planar supercell size in FD SCF calculations

AA' Structure

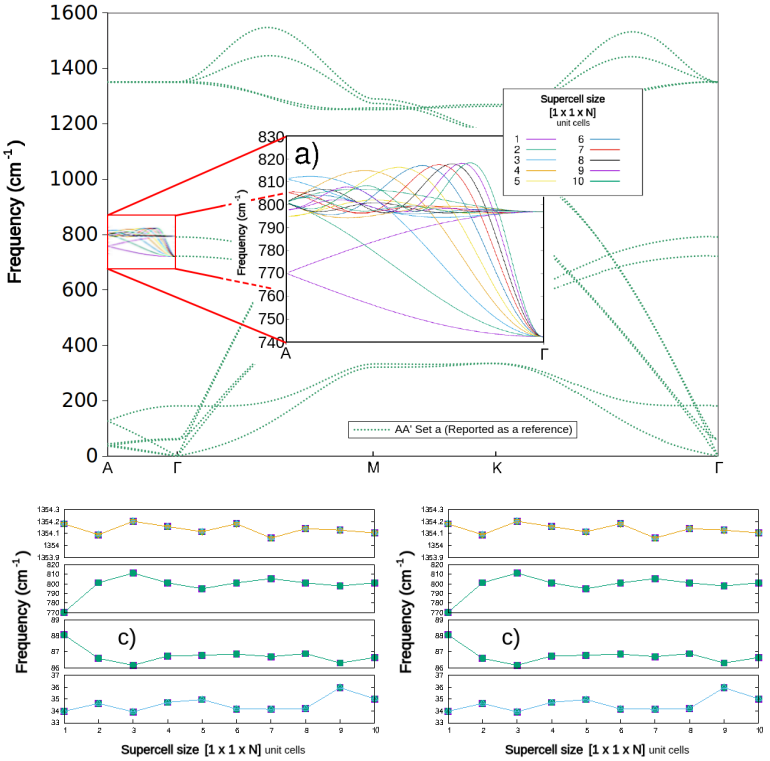

FIG. S18: Phonon energy dispersions for the h-BN AA' structure with varying supercell size in the z direction, perpendicular to the h-BN sheet, (a) along the $A-\Gamma$ high symmetry direction in the first Brillouin zone, (b) in the Γ point and (c) in the A point. Calculations performed with PAW-PBE and D3BJ van der Waals dispersion correction, FD value of 0.015 Å, see further computational details in E.S.I. Table TSI (cell parameters obtained with PAW-PBE-D3BJ, reported in Table TSII).

[1] M. Fuchs and M. Scheffler, Comput. Phys. Commun. **119**, 67 (1999).

[2] D. Hamann, M. Schlüter, and C. Chiang, Phys. Rev. Lett. **43**, 1494 (1979).

[3] D. Hamann, Phys. Rev. B **88**, 085117 (2013), corrected in [5].

[4] N. Troullier and J. L. Martins, Phys. Rev. B **43**, 8861 (1991).

[5] D. Hamann, Phys. Rev. B **95**, 239906 (2017).

[6] D. Vanderbilt, Phys. Rev. B **41**, 7892 (1990).

[7] A. Tkatchenko and M. Scheffler, Phys. Rev. Lett. **102**, 073005 (2009).

[8] S. Grimme, J. Comput. Chem. **27**, 1787 (2006).

[9] P. E. Blochl, Phys. Rev. B **50**, 1795 (1994).

[10] G. Kresse and D. Joubert, Phys. Rev. B **59**, 1758 (1999).

[11] J. Sun, R. C. Remsing, Y. Zhang, Z. Sun, A. Ruzsinszky, H. Peng, Z. Yang, A. Paul, U. Waghmare, X. Wu, *et al.*, Nat. Chem. **8**, 831 (2016).

[12] J. Sun, A. Ruzsinszky, and J. P. Perdew, Phys. Rev. Lett. **115**, 036402 (2015).

[13] H. Peng, Z.-H. Yang, J. P. Perdew, and J. Sun, Phys. Rev. X **6**, 041005 (2016).

[14] S. Grimme, S. Ehrlich, and L. Goerigk, J. Comput. Chem. **32**, 1456 (2011).

[15] H. Xu, J. Zhou, Y. Li, R. Jaramillo, and J. Li, Nano Res. **12**, 2634 (2019).

[16] H. Henck, D. Pierucci, Z. Ben Aziza, M. G. Silly, B. Gil, F. Sirotti, G. Cassabois, and A. Ouerghi, Appl. Phys. Lett. **110**, 023101 (2017).

[17] H. E. Çamurlu, S. Mathur, O. Arslan, and E. Akarsu, Ceram. Int. **42**, 6312 (2016).

[18] A. Hidalgo, V. Makarov, G. Morell, and B. Weiner, Dataset Papers in Science **2013** (2013).

[19] A. Mukheem, S. Shahabuddin, N. Akbar, A. Miskon, N. Muhamad Sarih, K. Sudesh, N. Ahmed Khan, R. Saidur, and N. Sridewi, Nanomaterials **9**, 645 (2019).

[20] L. Chen, H.-F. Xu, S.-J. He, Y.-H. Du, N.-J. Yu, X.-Z. Du, J. Lin, and S. Nazarenko, PloS one **12**, e0170523 (2017).

[21] X. Wang, Y. Xie, and Q. Guo, Chem. Commun. , 2688 (2003).

[22] J. Andujar, E. Bertran, and M. Polo, J. Vac. Sci. Technol. A **16**, 578 (1998).

[23] R. J. Nemanich, S. A. Solin, and R. M. Martin, Phys. Rev. B **23**, 6348 (1981).

[24] R. Geick, C. H. Perry, and G. Rupprecht, Phys. Rev. **146**, 543 (1966).

[25] S. Reich, A. C. Ferrari, R. Arenal, A. Loiseau, I. Bello, and J. Robertson,

Phys. Rev. B **71**, 205201 (2005).